THE ASTROPHYSICAL JOURNAL, 530:834–850, 2000 February 20

INFLUENCE OF MAGNETIC FIELDS ON PULSED, RADIATIVE JETS

T. A. GARDINER,[1] A. FRANK,[2] T. W. JONES,[3] AND D. RYU[4]

Received 1999 April 13; accepted 1999 October 4

ABSTRACT

We present results of magnetohydrodynamic simulations of steady and time variable jets for a set of conditions applicable to outflows from young stellar objects (YSOs). As a first step in a detailed study of radiative magnetohydrodynamic jets, we study both steady and pulsed jets with a large-scale magnetic field oriented parallel to the jet flow axis. While toroidal components may be present in many jets, we have chosen in this initial study to focus solely on pure poloidal initial geometries. The range of magnetic field strengths studied is characterized by the dimensionless parameter $\beta = 8\pi P_{\rm gas}/B^2 = 0.1$–$10^7$. The results of our simulations show that the global characteristics are not strongly dependent on the strength of the magnetic field. Instead, we find that a predominantly poloidal field has more subtle effects, such as inhibiting instabilities, and increasing the "order" in the flow patterns. While the fields act to restrict "turbulent" gas motions, the pulse-induced internal shocks increase the likelihood of instabilities, complicate the global flow patterns, and increase the likelihood of magnetic reconnection. We detail the ways in which the magnetic pressure and tension forces affect the kinematics observed in these simulations.

Subject headings: hydrodynamics — ISM: jets and outflows — MHD — shock waves — stars: magnetic fields — stars: pre–main-sequence

1. INTRODUCTION

After more than 30 years of study, a coherent, well-tested paradigm for HH objects has emerged. The emission in these bright knots, observed principally in visible forbidden and permitted lines, is known to result from recombination of shock-excited gas (as originally suggested by Schwartz 1975). The knots are often embedded in fainter, more extended jets. Typically, these stellar jets comprise a well-organized and well-collimated linear beam (with interruptions) extending from very small, less than 10 AU, to very large, sometimes parsec-length, scales (Reipurth, Bally, & Devine 1997). In some cases the HH objects and their parent jet appear as part of a larger outflow system, which may include a molecular outflow. In spite of the concord regarding the physical nature of HH objects, a consensus has not yet emerged about the exact nature of their origin or the information they convey about the star formation process.

Taken together, the ubiquity of HH objects, jets, and molecular outflows comprises one of the central challenges to the theory of star formation. Are these phenomena a pivotal means of regulating star formation, or are they merely a by-product of accretion? Because of limitations inherent in large distance, small size, and obscuration, most protostars (the central engines of the outflows) cannot usually be imaged directly. Given the long "look-back" or dynamical times $t_d = L_{\rm jet}/V_{\rm jet} \approx 10^3$–$10^5$ yr, the outflows may be one of the best means for recovering some sense of the history of star formation processes. Thus, understanding how each component of an outflow system arises and what it tells us about the basic physics and history of star formation remains a critical task. It is hoped that explication of the processes involved in the formation of HH objects, stellar jets, and molecular outflows will lead to an improved understanding of star formation physics, including star disk interactions, angular momentum losses and the mechanisms that conspire to determine the ultimate mass of a star.

Although a consensus has yet to emerge, the specific origin of HH objects is a question for which both theory and observation appear to be converging toward a unique answer. Currently two main classes of model exist, both of which interpret the HH objects as shock-bounded knots inside a collimated hypersonic jet beam. The first class of model (Bührke, Mundt, & Ray 1988) suggests that the knotty appearance of young stellar object (YSO) jets is caused by Kelvin-Helmholtz (KH) pinch-mode instabilities. This could be generalized to suggesting that the source of the knotty appearance of YSO jets is due to an instability induced in the flow during the jet propagation. The excitation of pinch-mode KH instabilities (Micono et al. 1998) and nonaxisymmetric KH modes (Stone, Xu, & Hardee 1997) have been studied both analytically and numerically. KH pinch-mode instabilities typically lead to a periodicity too rapid to match observations. Nonaxisymmetric KH modes do, however, appear to be a viable option for describing the gentle wandering or wiggling of the jet beam. The second class of models for HH objects (Rees 1978; Reipurth 1989) posits that the driving sources of YSO jets may be episodic or transient, changing on timescales much less than the dynamical timescale of HH objects. This has subsequently been referred to as an intrinsic variability, or instability, in the driving source. The resulting velocity variations lead to shock formation and knotty emission characteristics through nonlinear wave steepening. Reipurth based this conjecture on, among other things, the observation that some of the central stars associated with jets have been observed to suffer significant changes in

[1] Department of Physics and Astronomy, University of Rochester, Rochester, NY 14627-0171; gardiner@pas.rochester.edu.

[2] C. E. K. Mees Observatory and Department of Physics and Astronomy, University of Rochester, Rochester, NY 14627-0171; afrank@pas.rochester.edu.

[3] Department of Astronomy, University of Minnesota, Minneapolis, MN 55455; twj@msi.umn.edu.

[4] Department of Astronomy and Space Science, Chungnam National University, Daejeon 305-764, Korea; ryu@sirus.chungnam.ac.kr.

brightness—the so-called FU Orionis outbursts. Recently, the conjecture of intrinsic variability has received supporting evidence in the observations of HH 212 (Zinnecker, McCaughrean, & Rayner 1998). It is argued by Zinnecker et al. that the high degree of inversion symmetry observed in this jet is compelling evidence favoring intrinsic variability in the source of YSO outflows. The effects of jet variation or pulsation on a purely hydrodynamic jet has been studied by a number of authors (Raga et al. 1990; Raga & Kofman 1992; Stone & Norman 1993; de Gouveia Dal Pino & Benz 1994; Smith, Suttner, & Zinnecker 1997). These studies have found a good deal of agreement between theory and observations, lending additional support to the conjecture of jet source variability.

While much work has been done on the propagation of hydrodynamic jets, comparatively little work has been done on jets with dynamically important magnetic fields. This observation is in stark contrast to the general consensus in the astrophysics community that magnetic fields are primarily responsible for launching and collimation of YSO jets. The most popular magnetohydrodynamic (MHD) models rely on a combination of magnetocentrifugal forces in either an accretion disk ("disk winds": Blandford & Payne 1982; Königl 1989; Ouyed & Pudritz 1997) or at the disk-star boundary ("X-winds": Shu 1997). With regard to hydrodynamic jets, many studies have been done on collimation (Cantó & Rodríguez 1980; Frank & Mellema 1996; Delamarter, Frank, & Hartmann 2000), instabilities, and source variability as mentioned earlier. Thus the hydrodynamic behavior of jets is generally well understood. MHD collimation models have also been quite successful in articulating the physical properties of the launching process. Indeed, numerical simulations (Ouyed & Pudritz 1997; Romanova et al. 1998; Kudoh, Matsumoto, & Shibata 1998), have recently demonstrated the ability of disk-wind models to produce both steady and time-dependent jets. Thus hydrodynamic and magnetohydrodynamic collimation models have been well studied, as have hydrodynamic jet propagation models. What remain to be done are detailed numerical models of radiative MHD (RMHD) jets. To date only a few studies of RMHD jets (Frank et al. 1998; Cerqueira, de Gouveia Dal Pino, & Herant 1997) have been carried out.

While the direct observation of magnetic fields in jets is difficult, there is evidence that such fields exist, at least close to the star. Based on polarization measurements, Ray et al. (1997) claim to observe magnetic fields of order 1 G in an outflow of order 10 AU from T Tauri S. For typical jet parameters such a field strength would give a plasma $\beta = 8\pi P_{\rm gas}/B^2$ of $\beta \approx 10^{-11}$ to 10^{-7}. These values are so small that if they reflect global values in the jet, one could not really consider the system to be hydrodynamic at all. The plasma would be forced to follow the motion of the magnetic field lines as the magnetic field attempted to arrange itself into a force-free configuration. The authors conclude that the high values of B must come from regions of strong field amplification, such as behind shocks. One might reasonably ask, "If fields exist in the jets close to the source, then will they exist at larger distances?" As Frank et al. (1999) have recently shown, the ambipolar diffusion timescale for YSO jets can be estimated as

$$\tau_{\rm ad} \approx 28{,}904\left(\frac{n_n}{10^3\ {\rm cm}^{-3}}\right)\left(\frac{R_j}{10^{15}\ {\rm cm}}\right)^2\left(\frac{10^4\ {\rm K}}{T_j}\right)\left(\frac{\beta}{\beta+1}\right)\ {\rm yr}\ ,$$

where n_n is the neutral particle density, R_j is the jet radius, and T_j is the jet temperature. For jet parameters in the middle of the expected range of variation we find $\tau_{\rm ad}$ of order 10^4–10^5 yr. Therefore, while we expect that ambipolar diffusion may play a significant role in the long-term evolution of YSO jets, we can safely neglect its effects for the much shorter timescales of interest in this investigation. Given the importance of magnetic fields for jet launching and collimation, one would expect that hydromagnetic forces play a significant role in the propagation of YSO jets as well. Thus it is necessary to revisit all issues relevant to YSO jet propagation anew in light of the effects of magnetic fields.

In this paper we present the first study of pulsed, radiative, MHD jets. The numerical methods used to obtain these results are highlighted in § 2. The initial conditions, detailed in § 3, are chosen simple to facilitate a "clean" numerical study, e.g., we consider a pure B_z field embedded in both the jet and the ambient medium. Our goal here is to explicate if and how the dynamics of pulsed jets can change with the inclusion of magnetic fields and to determine whether the fields can provide new routes for channeling kinetic energy into thermal energy. In particular, Frank et al. (1997, 1998) pointed out that magnetic fields within the material dragged into the cocoon of a MHD jet would likely reconnect at some point. The high-resolution simulations presented in § 4 allow us to study this issue in some detail. We discuss these results in terms of previous models and observations in § 5 and summarize and draw conclusions in § 6.

2. NUMERICAL METHOD

We will present results obtained by numerically integrating the equations of ideal MHD, modified to include cooling due to optically thin radiative losses. The simulations are carried out in cylindrical coordinates (r, ϕ, z) with cylindrical symmetry and inversion symmetry across the $z = 0$ plane. Thus, the simulations follow a quarter-meridional plane ($r \geq 0$, $\phi = 0$, $z \geq 0$). Symmetry dictates the use of reflecting boundary conditions at the $z = 0$ plane and at the $r = 0$ line. We utilize outflow boundary conditions at the outermost radial and z boundaries. During the tests which we have run we have found little evidence of incorrect reflections from the $r = 0$ line due to the coordinate singularity, although it must be admitted that this problem plagues all numerical codes in cylindrical coordinates to some extent. The modified equations of MHD take the following form:

$$\frac{\partial \rho}{\partial t} + \frac{1}{r}\frac{\partial}{\partial r}(r\rho v_r) + \frac{\partial}{\partial z}(\rho v_z) = 0\ , \tag{1}$$

$$\frac{\partial \rho v_r}{\partial t} + \frac{1}{r}\frac{\partial}{\partial r}(r\rho v_r^2 - rB_r^2) + \frac{\partial}{\partial r}(P^*) + \frac{\partial}{\partial z}(\rho v_r v_z - B_r B_z) = \frac{\rho v_\phi^2 - B_\phi^2}{r}\ , \tag{2}$$

$$\frac{\partial \rho v_\phi}{\partial t} + \frac{1}{r}\frac{\partial}{\partial r}(r\rho v_\phi v_r - rB_\phi B_r) + \frac{\partial}{\partial z}(\rho v_\phi v_z - B_\phi B_z) = \frac{B_r B_\phi - \rho v_\phi v_r}{r}\ , \tag{3}$$

$$\frac{\partial \rho v_z}{\partial t} + \frac{1}{r}\frac{\partial}{\partial r}(r\rho v_z v_r - r B_z B_r) + \frac{\partial}{\partial z}(\rho v_z^2 - B_z^2 + P^*) = 0 , \quad (4)$$

$$\frac{\partial B_r}{\partial t} + \frac{\partial}{\partial z}(v_z B_r - v_r B_z) = 0 , \quad (5)$$

$$\frac{\partial B_\phi}{\partial t} + \frac{1}{r}\frac{\partial}{\partial r}(r v_r B_\phi - r v_\phi B_r) + \frac{\partial}{\partial z}(v_z B_\phi - v_\phi B_z) = \frac{v_r B_\phi - v_\phi B_r}{r} , \quad (6)$$

$$\frac{\partial B_z}{\partial t} + \frac{1}{r}\frac{\partial}{\partial r}(r v_r B_z - r v_z B_r) = 0 , \quad (7)$$

$$\frac{\partial E}{\partial t} + \frac{1}{r}\frac{\partial}{\partial r}[r(E + P^*)v_r - r B_r(\boldsymbol{B}\cdot\boldsymbol{v})] + \frac{\partial}{\partial z}[(E + P^*)v_z - B_z(\boldsymbol{B}\cdot\boldsymbol{v})] = -n_e n_i \Lambda(T) , \quad (8)$$

where the total energy and pressure are assumed to be well represented as an ideal gas, giving

$$P^* = P + \frac{1}{2}B^2 ,$$

$$E = \frac{1}{2}\rho v^2 + \frac{P}{\gamma - 1} + \frac{1}{2}B^2 .$$

In addition to the hyperbolic equations presented above, an additional constraint is imposed via the condition of flux conservation,

$$\frac{1}{r}\frac{\partial}{\partial r}(r B_r) + \frac{\partial B_z}{\partial z} = 0 .$$

The unit for the magnetic field in these equations is chosen for numerical purposes to be $(G/\sqrt{4\pi})$. Equations (1) and (8) describe conservation of mass and energy, respectively. The energy conservation equation includes a source term, $n_e n_i \Lambda(T)$, (where n_e and n_i represent the electron and ion number density), which models radiative losses in the optically thin limit. For $\Lambda(T)$ we use the Dalgarno-McCray "coronal" cooling curve (Dalgarno & McCray 1972) for the interstellar medium in a tabulated form. As we do not follow the ionization fraction directly in this work, we assume the gas to consist of fully ionized hydrogen ($n_e = n_i$) and shut off the radiative cooling below 10^4 K. Consistent with this assumption, we take the ratio of specific heats, $\gamma = 5/3$. Equations (2)–(4) represent conservation of momentum. Equations (5)–(7) are three components of the induction equation.

Specifically, the method we use to solve equations (1)–(8) is explicit, finite-volume, up-winded, conservative, second-order–accurate, and total variation diminishing (TVD). The code is conservative up to machine accuracy, ensuring that it will accurately capture shock strengths and speeds. Energy conservation ensures that the magnetic field energy lost during magnetic reconnection will be dissipated, modifying the thermal and kinetic energy. Magnetic reconnection only occurs in the simulations in regions of large current density. Thus it emulates reality when small, but finite, resistivity is present in a plasma. In this way, the code can be said to have a small but finite dissipation term built into the integration scheme, which may give some insight into the processes and consequences of magnetic reconnection. Various manifestations of the code have been reported in the literature in its one-dimensional Cartesian form (Ryu & Jones 1995), its two-dimensional Cartesian form (Ryu, Jones, & Frank 1995a), and its two-dimensional axisymmetric (cylindrical coordinates) form (Ryu, Yun, & Choe 1995b). The TVD property is ensured in the same way as was done originally by Harten for the Euler equations (Harten 1983). In the two-dimensional versions of the code, multidimensionality is handled through the use of Strang splitting (Strang 1968). The cooling is applied in a first-order fashion, as we have found minimal effects by incorporating the cooling with more expensive second-order accuracy. Finally, the crucial and problematic issue of maintaining $\nabla \cdot \boldsymbol{B} = 0$ is accomplished with a staggered-grid approach (Ryu et al. 1998). For more details the reader is directed to one of the above references, or for a general review of methods currently in use for integrating hyperbolic conservation laws, such as the Euler equations or ideal MHD equations see LeVeque (1992, 1997).

A note with regard to reconnection: the code used for these studies nominally treats the flows as "ideal," or non-dissipative. Dissipation does take place through numerical truncation and diffusion at the grid-cell level, i.e., primarily within the smallest resolved structures. The consistency of this approach with nonideal hydro flows of high Reynolds number has been convincingly demonstrated using turbulence simulations for conservative methods analogous to those employed here (e.g., Porter & Woodward 1994). While that comparison has not yet been accomplished for MHD flows, there are a number of results that support consistency for ideal MHD codes when the dissipation scales are small, as well. These include the apparent "convergence" in general flow and magnetic field patterns (as noted above) and global energy evolution seen in our own simulations mentioned above, as well as MHD turbulence studies (e.g., Mac Low et al. 1998; Stone, Ostriker, & Gammie 1998). Reconnection occurs through magnetic dissipation. We observe reconnection in our simulations, and while the specific mode of reconnection occurring is difficult to determine, it does occur when we would expect it (field reversals), in the manner expected (strong current sheets) and with the consequences expected (rapid conversion of magnetic to thermal energy).

3. SIMULATION PARAMETERS

The simulations follow a quarter-meridional plane ($r \geq 0$, $\phi = 0$, $z \geq 0$) with 300 grid cells, 2.5×10^{16} cm, in the radial direction and 1800 grid cells, 1.5×10^{17} cm, in the z-direction. The initial ambient medium will remain unchanged throughout the suite of simulations presented with a proton number density of $n_a = 60$ cm^{-3} and temperature $T_a = 10^4$ K. The subscript a, and similarly j, will be used to denote a property of the ambient and jet gas, respectively. Additionally, the ambient gas will be initialized at rest. The initial gas pressure in the jet is chosen such that $P_j = P_a$. To complete the specification of the jet gas properties, we set the value of η, the density ratio, giving $n_j = \eta n_a$ and $T_j = T_a/\eta$. The initial magnetic field is uniform and in the z-direction. The magnitude of the initial magnetic field is set by fixing the parameter β_i defined as $\beta_i = 8\pi P_a/B_z^2 = 8\pi P_j/B_z^2$. In Table 1 we have listed the properties of the simulations which we discuss in this paper. In this table M_{sj}

TABLE 1

SIMULATION PARAMETERS

Simulation	M_{sj}	M_{sa}	η	β_i	A[a]	τ_p[b]
Steady1.....	20	20	1	1.0	0.0	∞
Steady2.....	20	8.9	5	1.0	0.0	∞
Steady4.....	20	8.9	5	10^7	0.0	∞
Steady5.....	20	8.9	5	0.1	0.0	∞
Pulse1	20	20	1	1.0	0.25	57
Pulse1a.....	20	20	1	1.0	0.50	57
Pulse2	20	8.9	5	1.0	0.25	93
Pulse2a.....	20	8.9	5	1.0	0.50	93
Pulse4	20	8.9	5	10^7	0.25	93

[a] Pulse amplitude.
[b] Pulse period (yr).

and M_{sa} refer to the sonic Mach number obtained by comparing the speed of the jet and the sound speed in the jet and ambient medium, respectively.

The jet is injected at the $z = 0$ plane fully collimated, i.e., only the z-component of the velocity is nonzero. The jet is 60 grid cells wide, corresponding to a physical radius of 5.0×10^{15} cm. The jet is maintained during the simulation by treating it as a boundary condition in the "ghost cells." When initializing the simulation, the jet properties were copied into the first 10 grid cells to allow the code to resolve the forward and backward moving shocks on the grid in a natural way. We have found that for a jet with a uniform velocity in the z-direction, sometimes called a "top-hat" jet, the simulations develop instabilities at the radial boundary of the jet. We believe this to be a consequence of numerical round-off error seeding a Kelvin-Helmholtz unstable boundary. This problem is exacerbated by the use of a reflecting boundary condition at the $z = 0$ plane. For that reason we have chosen to give the in-flowing jet a velocity profile $v_0(r)$, which varies as an arctangent function, differing significantly from a "top-hat" profile in only the 10 or so outermost grid cells. The z-component of the velocity always remains superfast, ensuring that the jet inflow boundary conditions can be defined with impunity. To model the jet pulsation, we have chosen to vary the jet velocity sinusoidally as $v_j(r, t) = v_0(r)[1 + A \sin(2\pi t/\tau_p)]$. As the effects of varying the pulse period have been studied before (Stone & Norman 1993), we have chosen to fix the pulse period $\tau_p = t_{\rm cross}/5$, where

$$t_{\rm cross} = \left(\frac{L_z}{v_0}\right)\left(\frac{1+\sqrt{\eta}}{\sqrt{\eta}}\right)$$

is the estimated jet crossing time over the length of the grid, $L_z = 1.5 \times 10^{17}$ cm, in the z-direction.

4. RESULTS

4.1. *Steady Jets: Early Evolution*

In Figure 1 we present the density and magnetic field lines for the simulation Steady1, a jet with no pulsing, at quite an early time in the evolution of this jet. The density image shown in Figure 1 is very similar to what is observed for analogous hydrodynamic jets at similar times (Blondin, Fryxell, & Königl 1990). It is therefore quite striking to note that this simulation was initialized with an equipartition strength, $\beta_i = 1$, axial magnetic field. In fact, the formation

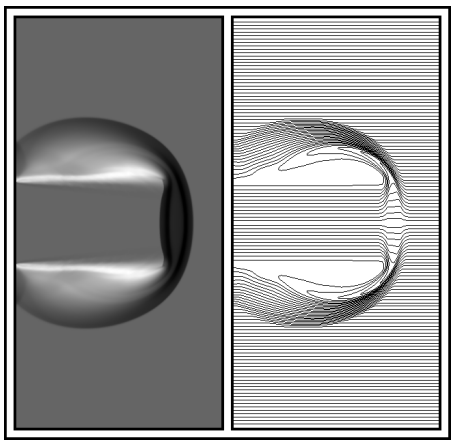

FIG. 1.—Logarithm of the density and magnetic field lines. The ion number density falls in the range of 3 cm^{-3} (*white*) to 440 cm^{-3} (*black*). The evolutionary time is 36 yr.

of this eye-shaped shock pair is quite ubiquitous to the simulations presented in this paper and plays an important role in the formation of magnetic field reversals, a prerequisite feature for the occurrence of reconnection. A detailed exposition of the kinematics involved in the formation and evolution of this shock pair is essential to the conclusions of this paper. Thus we will now present a self-contained description of the formation and evolution of the bow shock, jet shock, postshock gas, and embedded magnetic field shown in Figure 1.

The formation of this eye-shaped shock pair can be understood by considering the shock dynamics at early times for a top-hat jet with an axial magnetic field. Initially, the problem is one dimensional with a slipstream at the outermost radial boundary and thus will form the characteristic forward and reverse hydrodynamic shocks with a contact discontinuity between. The gas pressure between the forward and reverse shocks, or bow shock and jet shock, will be increased over that of the ambient medium, so that some δt after the shocks are formed a shock and rarefaction wave will respectively propagate outward and inward radially. The rarefaction wave lowers the gas pressure between the shock pair and induces an outward radial gas motion which draws the magnetic field lines out into the forming cocoon. The reduced postshock pressure increases the jet-shock speed and decreases the bow-shock speed at the edge of the jet compared to the axis, leading to the formation of oblique shock fronts. In turn, the oblique shock fronts redirect postshock ambient and jet gas in the positive radial direction, further reducing the postshock pressure and increasing the shock obliquity. This radial efflux of postshock gas continues until the bow shock and jet shock nearly collapse onto one another at the outermost radial edge, forming a quasi-equilibrium configuration, the eye-shaped shock pair shown in Figure 1. We refer to it as a quasi-equilibrium, simply because the effects of cooling have not been mentioned yet, but, as we will see, play a crucial role in the evolution of the system. With the introduction of pulsing, the same dynamics described here will occur with each pair of internal working surfaces, only on a smaller scale.

We can estimate the time required, $\tau_{\rm eq}$, for the radial pressure gradients, induced by the rarefaction wave, to

establish a quasi-equilibrium situation as being approximately equal to the time required for a magnetosonic wave to traverse the jet radius,

$$\tau_{\rm eq} = R_j \sqrt{\frac{4\pi\rho}{4\pi\gamma P + B_z^2}} \ .$$

Using values appropriate to the postshock region for this simulation, we obtain an estimate for $\tau_{\rm eq} \approx 20$ yr; for reference, the image shown was taken at 36 years. By this time, the jet shock has become sufficiently oblique at the outermost radial edge that the radial velocities of the postshock gas are as high as $\frac{1}{3}$ of the initial jet velocity. The shock pair will remain in the present configuration until the cooling becomes significant and the shock pair collapses. While the bow shock and jet shock remain spatially separated, the postshock gas will continue to drag the magnetic field lines into the cocoon.

The magnetic field was incorporated into the above description of the postshock dynamics as a passive local property of the gas. To justify this point of view and clarify the role played by the embedded magnetic field during its expulsion into the cocoon, we must consider the postshock region in some detail. As stated earlier, initially the bow shock and jet shock, or shock pair, are hydrodynamic shocks. Thus at very early times we may estimate the postshock properties from the familiar strong shock ($M_1 \gg 1$) relations (Landau & Lifshitz 1997),

$$\frac{T_2}{T_1} \approx \frac{2\gamma(\gamma-1)M_1^2}{(\gamma+1)^2} \ , \quad \frac{P_2}{P_1} \approx \frac{2\gamma M_1^2}{\gamma+1} \ , \quad \frac{\rho_2}{\rho_1} \approx \frac{\gamma+1}{\gamma-1} = 4 \ . \quad (9)$$

The subscript 1 and 2 refer to the plasma upstream and downstream of the shock, and M_1 is the sonic Mach number in a reference frame moving with the shock front. As a first approximation, these relations remain valid as long as the shocks are approximately "normal." We note also that the shocks in our simulations are too strong to become the switch-on type ($M_f > 2$; Ouyed & Pudritz 1993). To calculate the postshock properties we need an estimate for the velocity of the jet head. It is observed in the numerical simulations of steady jets that the jet quickly approaches a constant propagation speed and, for radiative jets, that the bow shock and jet shock remain relatively close to each other. Assuming these observations to be generally true, we transform to a coordinate system moving at the speed of the jet head and construct a closed Gaussian surface around the jet head with surfaces at $z = a$ (in the jet beam), $z = b$ (in the ambient medium), and $r = R_j$ (at the jet radius). Integrating equation (4) over the volume bounded by these surfaces, we obtain, for a top-hat, pressure-matched jet,

$$[\rho_j(v_j - v_h)^2 - \rho_a v_h^2] = \frac{2}{R_j}\int_a^b \left(\rho v_z v_r - \frac{B_z B_r}{4\pi}\right) dz \ ,$$

where we have assumed that the net z-momentum in the jet beam remains unchanged during its propagation toward the terminal working surface and returned to Gaussian units. The remaining integral describes the flux of z-momentum through the radial boundary at $r = R_j$. Note, however, that the distance between the bow shock and jet shock at the outermost radial boundary is much smaller than the jet radius. In addition, for the high Mach number jets considered here the terms $\rho v_z v_r$ and $B_z B_r$ in the integral are small compared to $\rho_a v_h^2$. Thus we may, to a good approximation, neglect the right-hand side of the above relation, and we recover the well-known relation (Norman, Winkler, & Smarr 1983) for the velocity of the jet head,

$$v_h = \left(\frac{v_j\sqrt{\eta}}{1+\sqrt{\eta}}\right). \quad (10)$$

Under these approximations we find that the magnetic field will not influence the jet propagation speed. We note that in the case of strong toroidal magnetic fields, Frank et al. (1998) calculated the modification to equation (10) due to an imbalance in the total (gas plus magnetic) pressure. The result shows only a weak dependence on the magnetic field.

Together, equations (9) and (10) predict that for simulation Steady1 the initial temperature $T_1 = 10^4$ will jump up to $T_2 = 3.1 \times 10^5$ K, and that the postshock pressure will be 125 times larger than the preshock pressure, in very good agreement with the simulation. Estimating the cooling timescale, we find $t_c \approx 30$ years, showing that cooling is important in this simulation. While the shocks remain approximately "normal," the magnetic field is only weakly affected by the shock waves. Under these circumstances we expect to find the dimensionless parameter $\beta = 8\pi P_{\rm gas}/B^2 \approx 100$ in the postshock region even though it was initialized to 1. Simulations show this to remain a good estimate even at the time at which Figure 1 was recorded. We conclude that for axial magnetic fields with $\beta > 0.01$ in the jet beam, the dynamics of the postshock gas will be dominated by hydrodynamic forces.

The dynamics of the gas in the postshock region is itself a very interesting phenomenon. If we follow the motion of the gas between the shock pair from the z-axis outward radially we see that the gas is forced to follow a converging flow pattern. Examining the radial gas velocity we find that the gas is subsonic near the z-axis with a radial gas velocity that increases as the flow is constricted. At $r \approx R_j$ the gas passes through the sonic point and undergoes supersonic expansion into the cocoon. This same feature is seen by considering the sonic Mach number of the gas in a reference frame moving with the jet head. Thus the shock pair and postshock gasdynamics offers an elegant example of a de Laval nozzle with an embedded magnetic field caught in the flow. The expulsion of postshock gas into the cocoon continues until cooling depletes the thermal energy between the shock pair to such an extent that the bow shock and jet shock collapse onto one another. When this occurs, the magnetic field lines become pinched, forming an X-type singularity which suffers magnetic reconnection. In our simulations, at least, this cooling-induced reconnection appears to be one basic process by which magnetic reconnection may occur.

As the postshock gas expands into the cocoon, both the gas pressure and magnetic field strength are reduced, though not at the same rate. This leads to an increase of β to $\approx 10^4$ in the cocoon of the present simulation. Thus the dynamics of the gas in the cocoon, like the postshock gas between the shock pair, is predominantly controlled by the hydrodynamic features of the flow, and the magnetic field is forced to follow along. In the cocoon and the region between the shock pair we also observe magnetic reconnection; however, here it is not driven by cooling. By studying the evolution of the magnetic field lines, we find that the gas in these regions is susceptible to "driven" reconnection. That is, the complex motion of the gas can fold the magnetic

field lines over and squeeze them together, and the Lorentz force is too weak to prevent the inevitable reconnection. Since those configurations are "tearing mode"–unstable, many local sites of reconnection can develop, so that reconnection is very fast (e.g., Jones et al. 1997).

4.2. *Steady Jets: Role of β*

Next, in Figures 2*a* and 2*b* we compare the evolved state of three steady, overdense jets, simulations Steady5, Steady2, and Steady4. These differ only in the value of $\beta_i = 0.1$, 1.0, and 10^7. Our intention is to study how the inclusion of dynamically significant axial magnetic fields modifies the long-term characteristics of an MHD jet compared to a hydrodynamic jet by varying the strength of the magnetic field. Our results show numerous differences between strong-field and weak-field simulations which can be understood as a consequence of the Lorentz force, or, equivalently, magnetic pressure and tension forces. To wit, using Ampère's law (neglecting the displacement current), the Lorentz force may be rewritten as

$$\frac{1}{c}(\boldsymbol{J}\times\boldsymbol{B}) = \frac{-1}{4\pi}\boldsymbol{B}\times(\nabla\times\boldsymbol{B}) = \frac{(\boldsymbol{B}\cdot\nabla)\boldsymbol{B}}{4\pi} - \nabla\left(\frac{B^2}{8\pi}\right). \tag{11}$$

In the final expression, the first and second term are often called the magnetic tension force and pressure force, respectively. It is often argued that this form is preferable, since the magnetic pressure term can be added to the gas pressure, effectively changing the equation of state, leaving the Lorentz force as being caused by the tension term alone. This separation is artificial, however, since the two terms just defined as the pressure and tension are not independent; after all, the Lorentz force is always orthogonal to the magnetic field, since $\boldsymbol{B}\cdot(\boldsymbol{J}\times\boldsymbol{B}) = 0$. This can be made

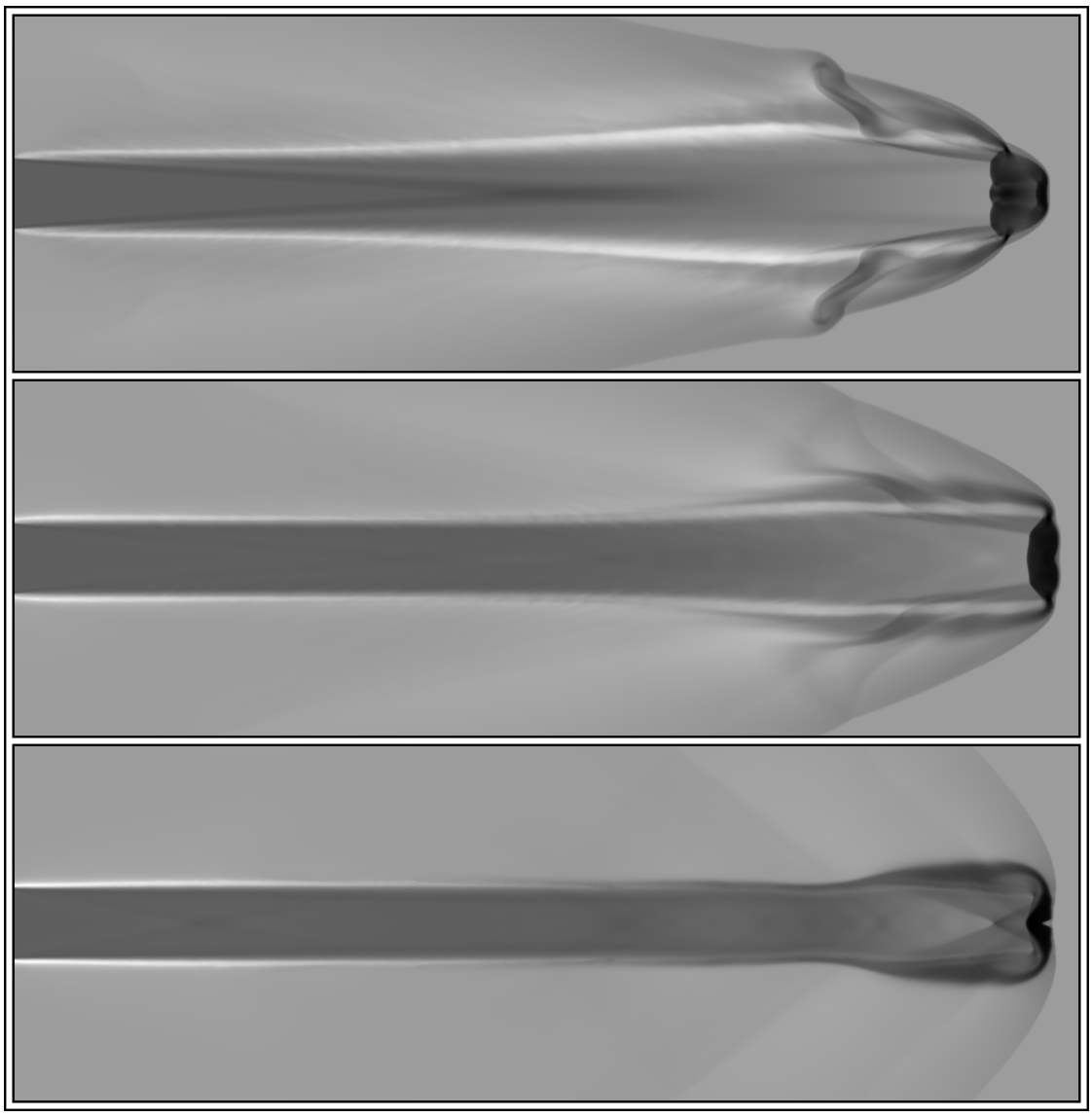

FIG. 2*a*

FIG. 2.—(*a*) Logarithm of the density for simulations Steady4, Steady2, and Steady5 (*from top to bottom*). The initial magnetic field strength increases from top to bottom. The ion number density falls in the range of 5 cm^{-3} (*white*) to 3.6 × 10^2 cm^{-3} (*black*). From top to bottom the evolutionary times are 441, 464, and 464 yr. (*b*) Magnetic field lines for simulations Steady4, Steady2, and Steady5 (*from top to bottom*). The initial magnetic field strength increases from top to bottom. From top to bottom the evolutionary times are 441, 464, and 464 years.

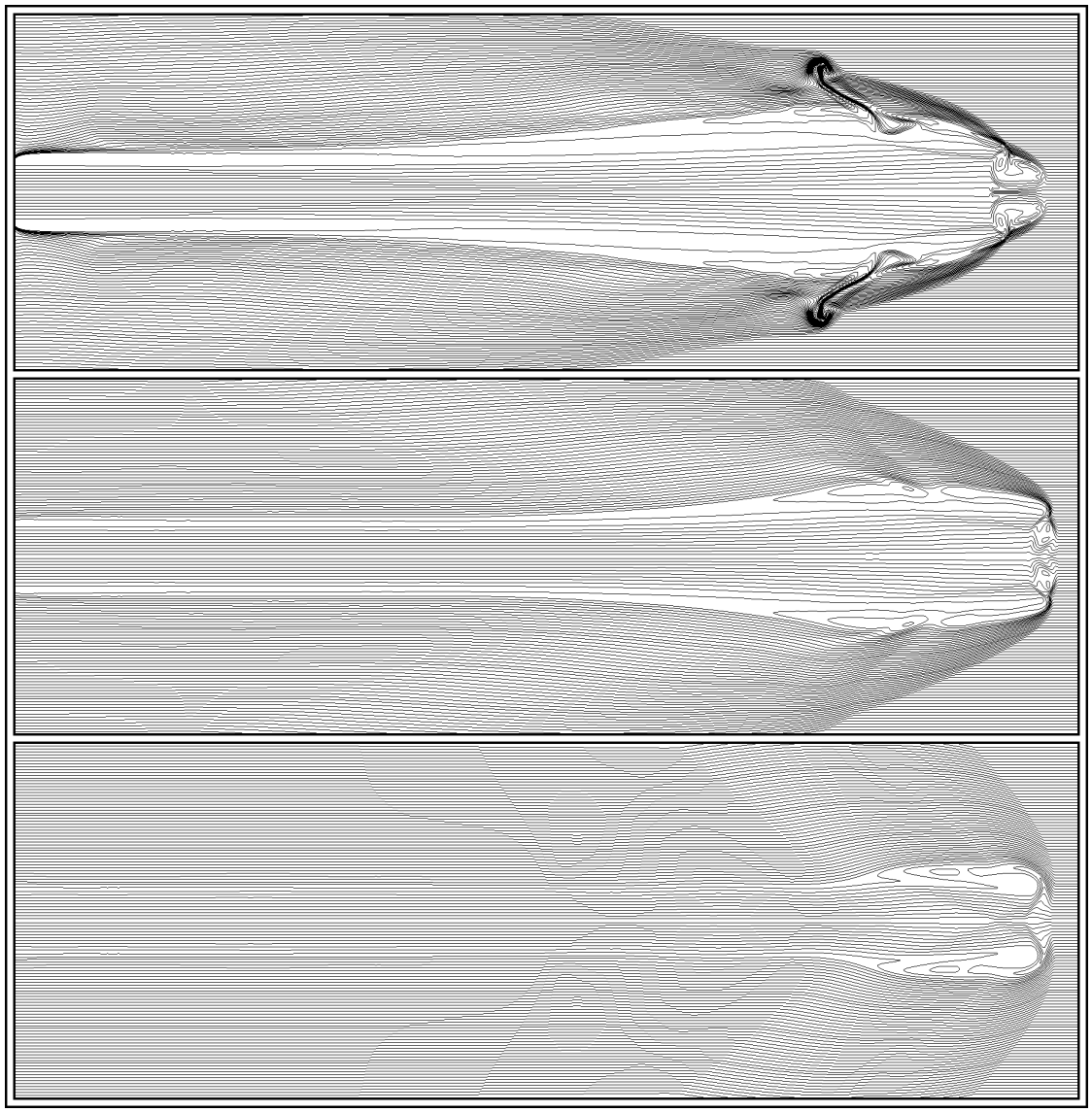

FIG. 2*b*

explicit by rewriting the Lorentz force as follows:

$$\frac{1}{c}(\boldsymbol{J}\times\boldsymbol{B}) = \frac{B^2}{4\pi R}\,\hat{\boldsymbol{n}} - \boldsymbol{\nabla}_{\perp}\left(\frac{B^2}{8\pi}\right), \tag{12}$$

where $\hat{\boldsymbol{n}}$ is a unit vector directed toward the local center of curvature of the field line, R is the local radius of curvature, and $\boldsymbol{\nabla}_{\perp}$ is the gradient operator in the two directions orthogonal to the magnetic field. We will refer, henceforth, to the first and second term in *this* expression for the Lorentz force as the magnetic tension and pressure force, respectively. In this form it is immediately apparent that the tension force attempts to straighten out the magnetic field lines, while the pressure force attempts to make the magnetic field strength uniform. Comparing the simulations presented in Figures 2*a* and 2*b* in light of equation (12), many differences become apparent in both the density and the magnetic field lines, whose origin must ultimately be traced back to the only difference in their initial conditions, the strength of the magnetic field.

We first consider the jet head, the most dynamic region in the three simulations, and note that the maximum density values in each jet are quite comparable. This can be understood by recognizing that in a uniform MHD fluid the easiest direction in which one may compress the fluid is parallel to the magnetic field, since, for small displacements, the Lorentz force has no influence. This is also consistent with the finding that the density is a maximum near the z-axis in each simulation, where the magnetic field lines, by symmetry, must be nearly parallel to the z-axis. The second trend we see in Figure 2*a* is the steady decrease in the stand-off distance, or the distance from the bow shock to the jet shock, as the initial magnetic field strength is increased. During the evolution of these jets, the jet shock is subjected to perturbations in the jet beam due to the beam's interaction with the hot slipstream and cocoon. Waves generated in the interaction produce distortions in the jet shock, turning its normal oblique to the jet velocity. The oblique jet shock gives rise to higher postshock velocities and shock focusing. This shock-focused gas competes with the Lorentz force in determining its postshock motion. For the weak magnetic field simulation the gas momentum is dominant, which leads to vortical motions in the region between the shock pair. This "turbulence" in the region

between the shocks creates a dynamic pressure and increases the stand-off distance. As the initial magnetic field is strengthened, the turbulence is inhibited by the tension associated with the field. This view is supported by the magnetic field line images in Figure 2*b*, which show increasingly twisted magnetic field lines as the initial strength of the magnetic field is reduced. It is also consistent with the relative dynamical importance of the field as measured by the parameter β in the postshock region.

Simulations Steady4, Steady2, and Steady5 were initialized with β_i equal to 10^7, 1.0, and 0.1. After propagation the value of β in the jet head falls in the range 10^7–10^{14}, 1–10^4, and 0.5–10^2, respectively. Thus even in the strongest field simulations where the influence of magnetic stresses has clearly altered the propagation characteristics, there are regions where the field would appear to be dynamically weak. It is important, however, to note that the β parameter does not measure the effect of tension forces, which will depend critically on the local topology of the field. Thus we conclude from this comparison that the influence of a magnetic field on the jet head can be complex and will depend critically on both the strength and orientation of the magnetic field.

We turn now to the cocoon formed by the radial expulsion of postshock gas from between the shock pair. The postshock values of β just quoted for the three simulations demonstrate that the magnetic fields may have an influence on the postshock dynamics for the $\beta_i = 0.1$ simulation. As β_i is reduced, we see from both the density and magnetic field line images that the presence of a strong axial magnetic field inhibits the growth of instabilities in gas ejected from the shock pair. This inhibition is effected primarily by tension forces that constrain motions which would draw out and bend field lines as material flows into the cocoon.

Note in the simulations that as the magnetic field strength is increased, the likelihood of magnetic reconnection, as measured by the number of closed field lines in Figure 2*b*, is reduced. We can understand this trend by imagining the evolution of the magnetic field as it is first folded over to form a field reversal or an X-point. Only then can the field line suffer magnetic reconnection. The tension force associated with the magnetic field inhibits the folding over or reversal of the magnetic field. This picture is consistent with the increasingly straight and uniform magnetic field lines seen in Figure 2*b* as the initial field strength is increased. Thus the presence of a strong magnetic field increases the "order" in the simulation. Similarly, as one considers increasing field strengths there is a range in which magnetic reconnection is likely, but also where magnetic tension is sufficient to induce "self-organization." That is, the local cross helicity, measured by $\hat{\boldsymbol{v}} \cdot \hat{\boldsymbol{B}}$, is increased.

Finally, note the general trend of a widening bow shock as the magnetic field strength is increased. This effect owes its origin to the increased magnetosonic wave speed, and is interesting in light of the attempts to explain molecular outflows as being driven by YSO jets. However, we must be careful not to misinterpret this increase in the wave speed as indicating an increase in the mass flux through the outermost radial boundary. In fact, just the opposite occurs, as the reader may readily confirm by counting the number of field lines that cross the radial boundary of the grid. As the magnetic field strength is increased, fewer and fewer field lines cross the outermost radial boundary. Since the gas is tied to the field, increasing the strength of the axial magnetic field decreases the mass flux through the outermost radial boundary of the grid. Generally speaking, for $\beta_i \lesssim 0.1$ the jet propagation is becoming sufficiently one-dimensional that it is beginning to resemble siphon flows in magnetic flux tubes (Thomas 1988).

4.3. *Pulsed Jets: Shock Formation and Interaction*

We turn now to the study of pulsed MHD jets with axial magnetic fields. In Figures 3*a* and 3*b* we show the evolution of the density and magnetic field for an equal density, $\eta = 1$ simulation, Pulse1a. This simulation was initialized with an equipartition, $\beta_i = 1$ axial magnetic field, but many of the evolutionary characteristics are similar to hydrodynamic jets. As each pulse propagates onto the grid it gradually steepens to form a pair of shock waves, often referred to as internal working surfaces, which are the analogs of the bow shock and jet shock. Since gas ahead of any given internal working surface is in motion, the internal working surfaces will propagate at higher velocities than the jet head or terminal working surface, and will eventually collide with the jet head. The repetitive collisions between the internal and terminal working surfaces serve to resupply the terminal working surface with thermal energy which will be converted into radiation. For sufficiently high pulse amplitude this might lead to observable temporal variations in the brightness of the terminal working surface, albeit on a long timescale. The collision period would be shifted from the pulse period due to the relative motion of the internal working surfaces and the jet head. As an estimate of the collision period, consider the situation when the speed of the jet head, v_h, and the speed of the internal working surfaces, $v_{\rm iws}$, are constant, $v_{\rm iws} > v_h$, and the pulse period is τ_p. Then the time between collisions, or collision period τ_c, is

$$\tau_c = \tau_p \left(1 - \frac{v_h}{v_{\rm iws}}\right)^{-1} . \tag{13}$$

Loosely speaking, we should expect the collision period to increase with η, the density ratio. Unfortunately, this relation gives the pulse period, which for YSO jets is estimated to be on the order of 10 yr, as a lower bound to the collision period.

When the variation in the jet velocity is large compared to the variation in either the Alfvén speed or sound speed, a simple analysis using the inviscid form of Burgers's equation can accurately predict the time and location for a shock to form, as has been noted by previous authors (Smith et al. 1997; Raga & Kofman 1992 and references therein). We present a simple analytic treatment predicting the time and position at which the velocity variations will steepen into shock waves and find a closed-form solution for the velocity variations used in this study. We begin by considering a gas parcel which leaves the position $z = z_0$ at time t_0 with a velocity $v_j(t_0)$, and another gas parcel which leaves a short time δt later. A shock will form when these two gas parcels intersect, or when

$$(t - t\,)v_j(t_0) = (t - t_0 - \delta t)v_j(t_0 + \delta t) .$$

Rearranging these terms and taking the limit as δt goes to zero, we get the time t at which a gas parcel which leaves z_0 at time t_0 with a velocity $v_j(t_0)$ will form a shock with its neighbors. We find that

$$t - t_0 = \frac{v_j(t_0)}{v_j'(t_0)} \quad \text{and} \quad v_j'(t_0) = \frac{dv_j(t_0)}{dt_0} . \tag{14}$$

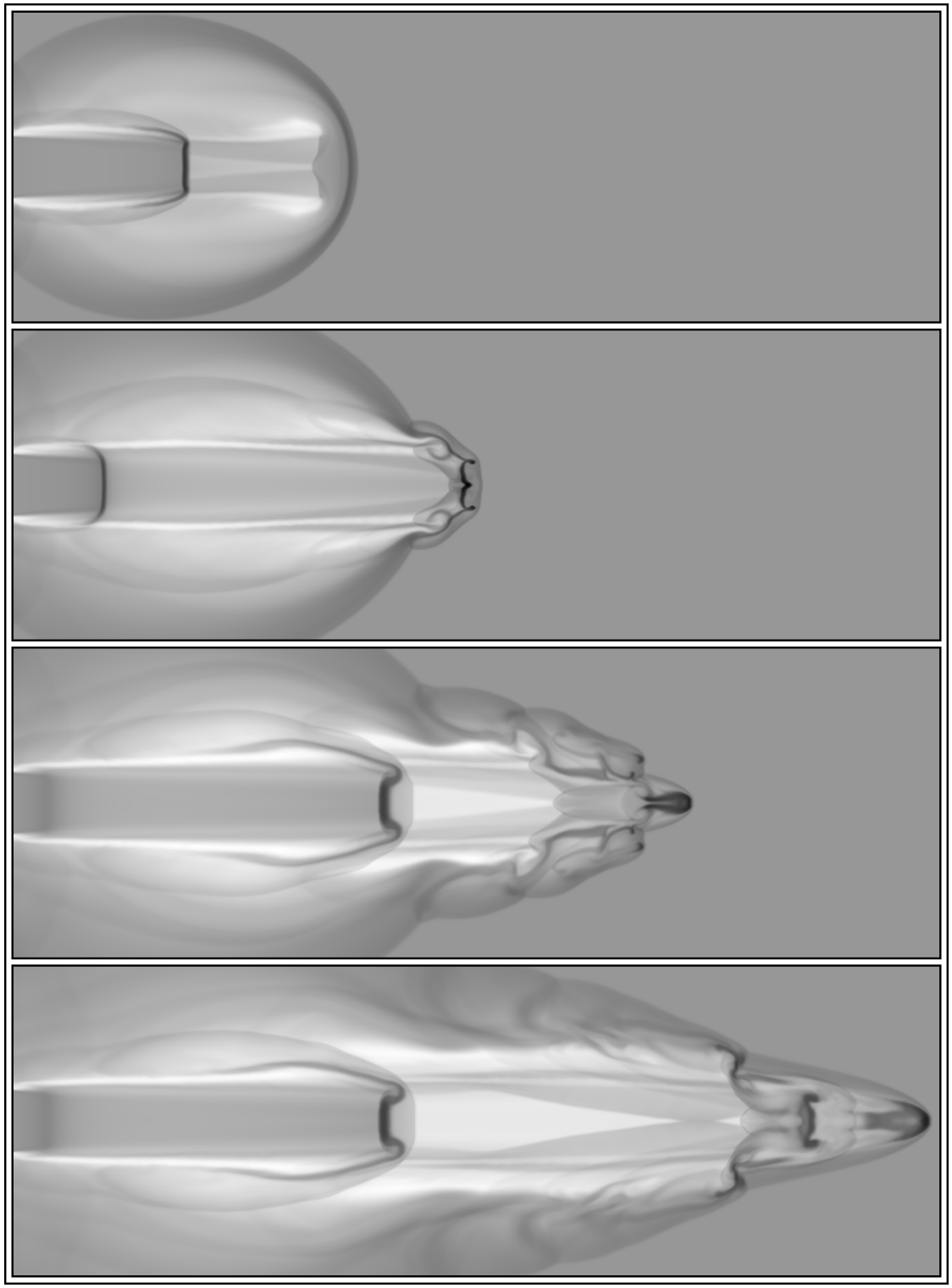

FIG. 3*a*

FIG. 3.—(*a*) Evolution of the logarithm of the density for simulation Pulse1a. The evolutionary times are 86, 129, 172, and 230 yr (*from top to bottom*). The ion number density falls in the range of 1 cm^{-3} (*white*) to 29.6 $\times$ 10^3 cm^{-3} (*black*). (*b*) Evolution of the magnetic field lines for simulation Pulse1a. The evolutionary times are 86, 129, 172, and 230 yr (*from top to bottom*).

Since $v_j(t_0) > 0$ and $t > t_0$, we must have $v_j'(t_0) > 0$ to form a shock. For $v_j'(t_0) < 0$ we will form a shock for $t < t_0$, i.e., rarefaction waves steepen to form shocks when time is reversed. Once a shock wave forms, the full set of ideal MHD equations are required to follow the dynamics. Therefore, from the above analysis we would prefer to know the earliest time at which a shock will form, or minimize t with respect to variations in t_0, which gives

$$2\{v_j'(t_0)\}^2 = v_j(t_0)v_j''(t_0) \; . \tag{15}$$

This tells us that since $v_j(t_0) > 0$ and $v_j'(t_0) > 0$ we must have $v_j''(t_0) > 0$ to have a minimum in t. Solving this equation

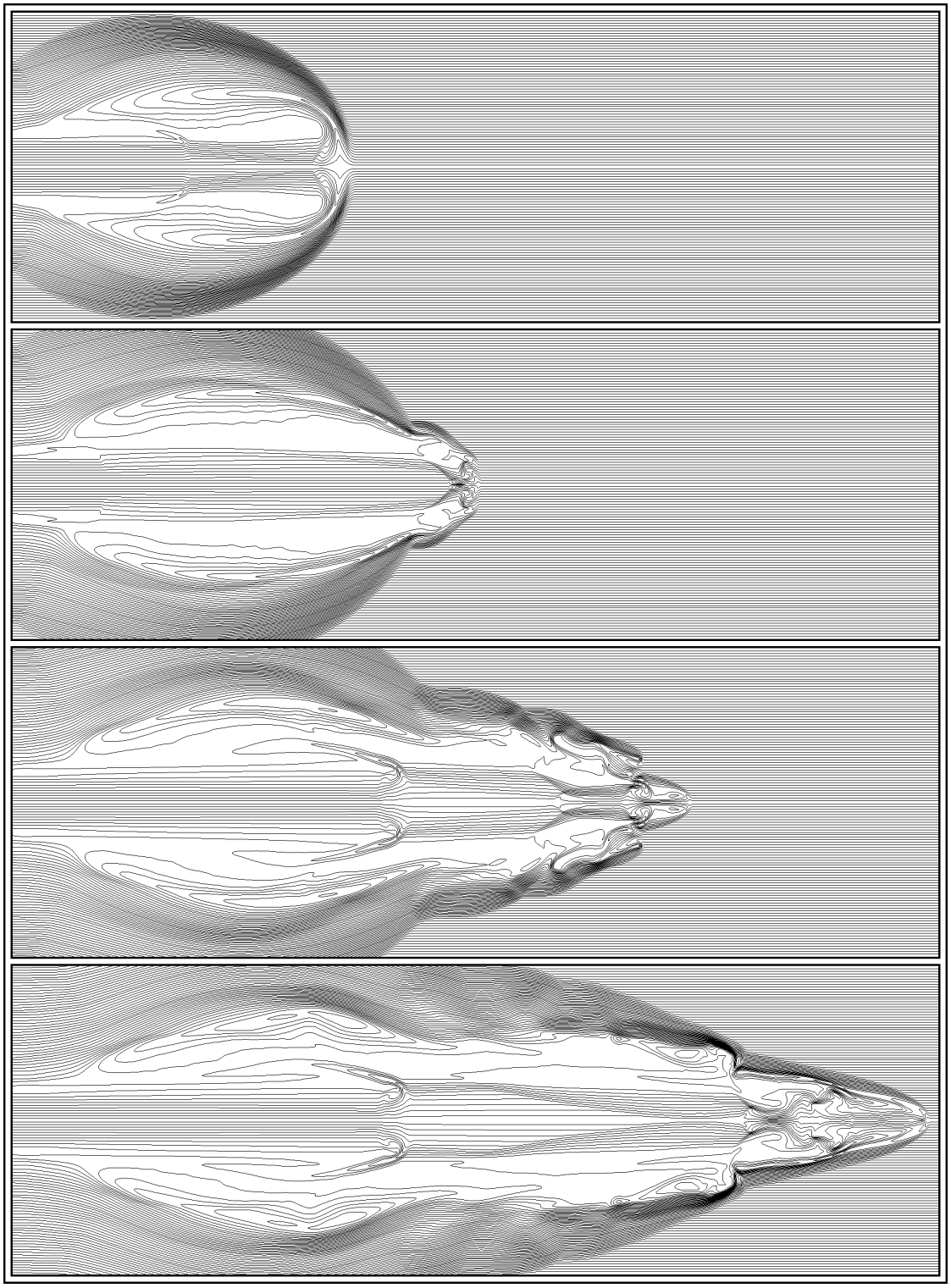

FIG. 3*b*

yields the time t_0 at which a gas parcel will leave z_0 and be the first to form into a shock with its neighbors. We now apply these relations to the specific jet velocity profile used in the this study, i.e.,

$$v_j(t) = \bar{v}[1 + A \sin(\omega t)] .$$

In what follows we choose A to be positive, and since $v_j(t) > 0$ we must have $A < 1$. Applying the constraints noted earlier, namely, $v_j'(t_0) > 0$ and $v_j''(t_0) > 0$, we find that $3\pi/2 < \omega t_0 < 2\pi$ modulo 2π. To determine t_0 more accurately, we need to solve equation (15), which for the chosen jet velocity profile is readily found to be a quadratic equation in terms of sin (ωt_0). The correct solution,

$$\sin(\omega t_0) = \frac{1 - \sqrt{1 + 8A^2}}{2A} , \tag{16}$$

is chosen by noting the requirement that $v_j''(t_0) > 0$. Making use of equation (14), we can calculate the time to shock formation,

$$t = \frac{1}{\omega} \sin^{-1}\left(\frac{1-\sqrt{1+8A^2}}{2A}\right) + \frac{3-\sqrt{1+8A^2}}{\omega[4A^2-(1-\sqrt{1+8A^2})^2]^{1/2}}, \quad (17)$$

which shows that the shock formation process will be periodic, as should be expected, with the period of the velocity variations. We can also calculate the distance that the gas parcel will travel before forming a shock:

$$z - z_0 = \left(\frac{\bar{v}}{2\omega}\right) \frac{(3-\sqrt{1+8A^2})^2}{[4A^2-(1-\sqrt{1+8A^2})^2]^{1/2}}. \quad (18)$$

We can use the above analysis and check for consistency with the dynamics observed in the simulations. We have compared the time and location at which a shock is formed in our simulations to the value predicted by the equations above, finding a very good agreement. For example, considering simulation Pulse1a, these formulae predict that a shock will first be formed at 124 yr and 751 AU from the bottom of the simulation grid. At 122 yr a very steep velocity front is located at 640 AU, though a shock has not yet developed. At 129 yr, as shown in Figure 3*a*, a well-developed shock pair is located at 950 AU. These nicely bound the location and time of shock formation in this simulation as well as the predicted values. We find similar agreement in all of the other simulations presented in this paper. In general, we estimate that the errors associated with using Burgers's equation to predict the time and location of shock formation are less than 5%.

Aside from the formation of shocks, the introduction of a velocity variation has incorporated new dynamics into the simulations. For example, making use of the equation of mass conservation one may show that velocity variations lead to compression and rarefaction of the jet beam during propagation. Raga & Cantó (1998) have independently performed a similar analysis to the one presented here and study the density jump across internal working surfaces. They show through both analytical and numerical means that sinusoidal velocity variations naturally lead to an increased density upstream and decreased density downstream of the shock. This is a general feature which should be expected whenever the velocity variations are periodic and continuous. Making use of the continuity equation, one may show that the density of a gas parcel ρ at time t which was launched at time t_0 with velocity $v_j(t_0)$ and density ρ_0 is given by

$$\rho = \frac{\rho_0}{1-k(t-t_0)}, \quad \text{where} \quad k = \frac{v_j'(t_0)}{v_j(t_0)}. \quad (19)$$

Considering the velocity variations studied in this paper, it follows that for $\cos(\omega t_0) < 0$ the gas will be rarefied, while for $\cos(\omega t_0) > 0$ the gas will be compressed. Simulations show that the portions of the jet pulse which suffer compression due to their velocity variation pass through the internal working surfaces on a timescale of the pulse period, leaving only the gas which suffers rarefaction separated by the internal working surfaces. We might estimate the time required for all of the gas that undergoes compression to pass through the internal working surfaces by asking when a gas parcel ejected at a time $\omega t_0 = 3\pi/2$ will collide with a gas parcel ejected at a time $\omega t_0 = 5\pi/2$. This yields

$$t - t_0 = \left(\frac{1+A}{4A}\right)\tau_p, \quad (20)$$

where τ_p is the pulse period. Note that this calculation ignores the presence of shock waves and is therefore only an estimate. For the pulse amplitudes studied here this time is on the order of the pulse period, in agreement with the simulations. Ignoring the pulse closest to the jet base, the jet beam consists of pairs of internal working surfaces separated by a rarefying beam. The upstream to downstream density contrast across internal working surfaces results from a simple fact. The gas downstream of the internal working surface has propagated for a longer time than the gas upstream of the internal working surface and therefore has a lower density. As described by Raga & Cantó (1998), this density contrast is a common feature of many HH objects in YSO jets.

The rarefaction, whose origin lies in the velocity variations, has additional consequences for jets with embedded magnetic fields. Since the velocity is parallel to the magnetic field, as long as the jet remains approximately in pressure balance with the surrounding gas, the magnetic field strength will remain constant. The decreasing gas density will lead to an increasing Alfvén speed, as well an adiabatic expansion that cools the gas, decreasing the parameter $\beta = 8\pi P_{\rm gas}/B^2$. Our simulations bear out this expectation. We find that in the regions of the jet beam between the internal working surfaces, β decreases with increasing z and can drop by as much as a factor of 20. The reduction in β and the Alfvénic Mach number should have important effects on the growth rate for Kelvin-Helmholtz instabilities, which depends on the Alfvénic Mach number.

Turning now to the magnetic field lines (Fig. 3*b*), we see that, as mentioned earlier, each pair of internal working surfaces evolves in a manner analogous to the bow shock and jet shock. The main difference between each pair of internal working surfaces and the (bow shock, jet shock) pair is the shock strengths. Since the gas in front of each pair of internal working surfaces is in motion, the shocks will be weaker and the postshock temperatures and pressures will be lower. Therefore, the cooling and radial expulsion of postshock gas into the cocoon will be lessened. For example, from the magnetic field lines at 86 years, one can see that just as the gas between the bow shock and the jet shock has been forced radially outward to form the cocoon, the internal working surfaces push gas radially outward as well, only on a smaller scale. Note that by 130 years the pulse, evident at 86 years, has collided with the jet shock, giving rise to small reconnection regions and quite a complicated shape of the jet head. The large loops of field lines ejected from between the bow shock and the jet shock suffer a reconnection event between 86 and 130 years, which leaves them isolated in the cocoon. Each jet pulse emitted subsequently to the formation of this magnetic island buffets it with the postshock gas ejected radially from between the internal working surfaces. This causes the islands to suffer enhanced dissipation as the simulation evolves. The routine we utilize to draw these magnetic field lines allows us to follow individual field lines from frame to frame. Thus the reader may follow the central field loop

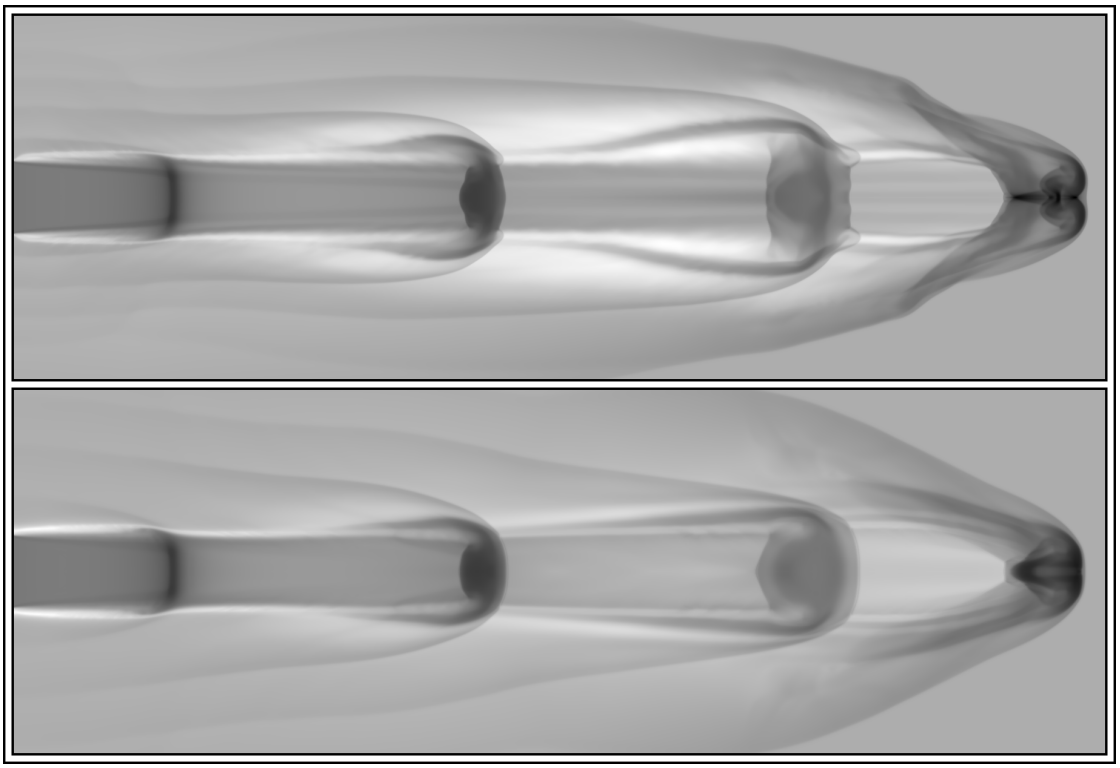

FIG. 4*a*

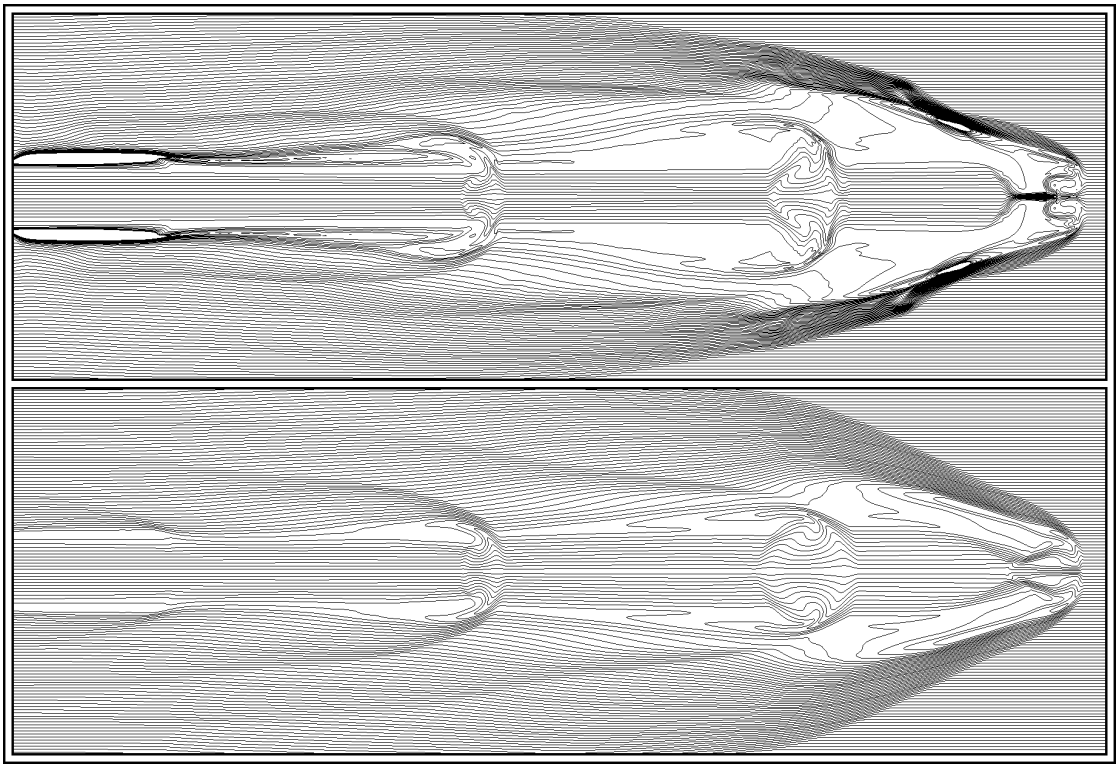

FIG. 4*b*

FIG. 4.—(*a*) Logarithm of the density for simulations Pulse4 (*top*) and Pulse2 (*bottom*) at an evolutionary time of 418 yr. The initial magnetic field strength increases from top to bottom. The ion number density falls in the range of 5 cm^{-3} (*white*) to 11.7 $\times$ 10^3 cm^{-3} (*black*). (*b*) Magnetic field lines for simulations Pulse4 (*top*) and Pulse2 (*bottom*) at an evolutionary time of 418 yr. The initial magnetic field strength increases from top to bottom.

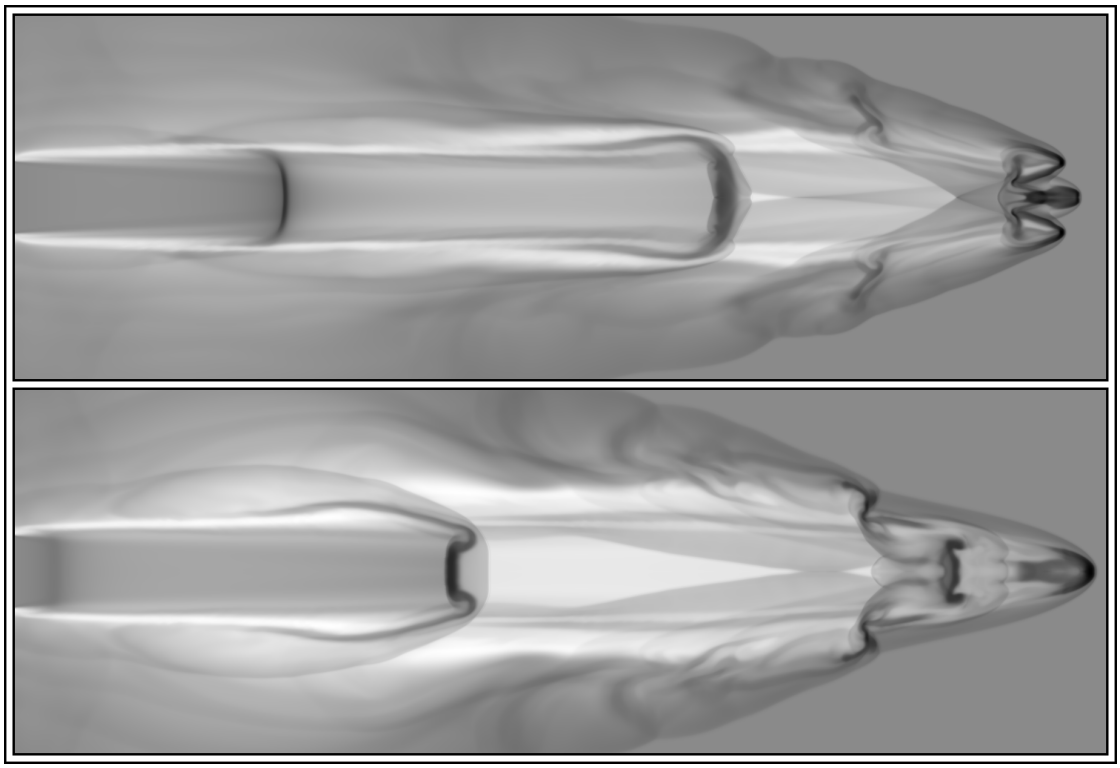

FIG. 5*a*

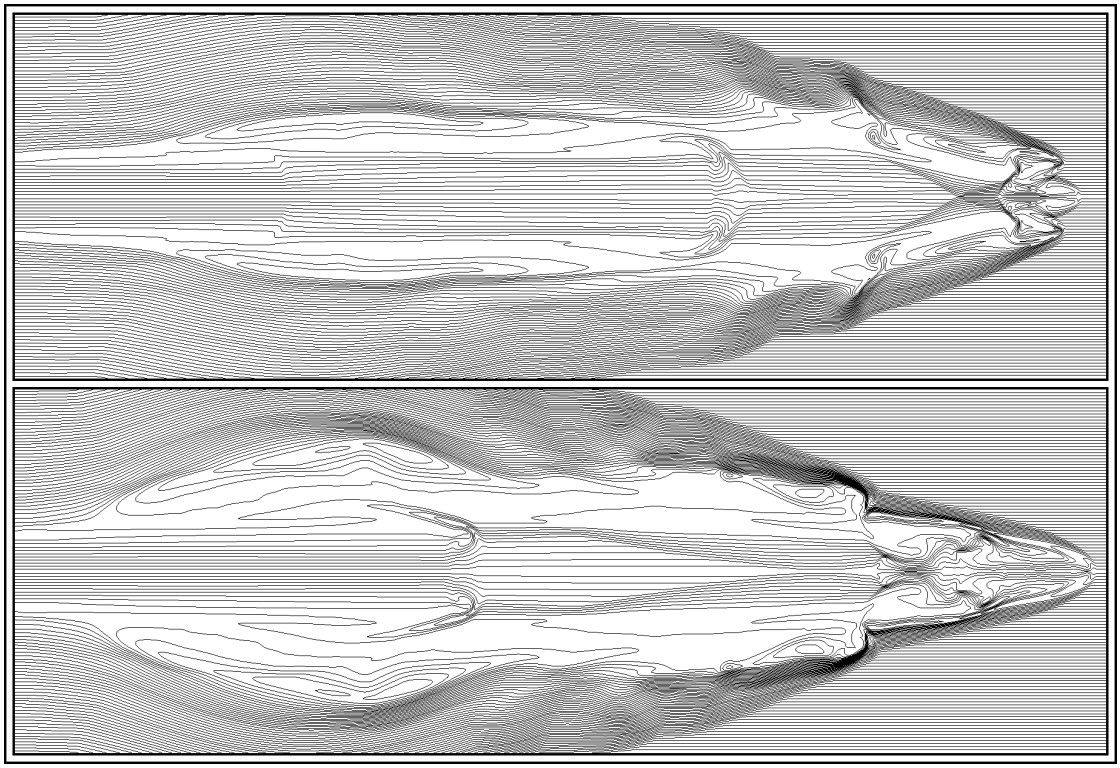

FIG. 5*b*

FIG. 5.—(*a*) Logarithm of the density for simulations Pulse1 (*top*) and Pulse1a (*bottom*) at evolutionary times of 266 and 229 yr, respectively. The ion number density falls in the range of 1 cm^{-3} (*white*) to 8.3×10^3 cm^{-3} (*black*). (*b*) Magnetic field lines for simulations Pulse1 (*top*) and Pulse1a (*bottom*) at evolutionary times of 266 and 229 yr, respectively.

shown at 130–230 yr, whereupon it has shrunk to a smaller size.

4.4. *Pulsed Jets: The Effect of β*

We turn our attention now to Figures 4*a* and 4*b*, comparing simulations Pulse2 and Pulse4, which differ only by the strength of the initial magnetic field. As shown in Table 1, these simulations are initialized with $\beta_i = 10^7$ and $\beta_i = 1$, respectively. The weak-field simulation is essentially a hydrodynamic jet, so that the comparison of these two simulations clearly shows which features of a pulsed jet are modified by the incorporation of an equipartition axial magnetic field. Notice that the general characteristics of the jet are only weakly modified. The internal working surfaces are at the same location in both jets, as is a crossing shock. The differences between the simulations are in the details.

Consider first the density for the two simulations. The maximum density in each simulation occurs in the head of the jet where the crossing shock pinches the gas toward the z-axis, but the maximum density in the weak-field simulation is approximately twice as large as in the $\beta_i = 1$ simulation. The difference in the gas compression due to the crossing shock is a consequence of the often-stated fact that magnetic pressure (proportional to B_z^2 in this case) can inhibit gas compression. This is in marked contrast with the results from the steady simulations (demonstrating the importance of the magnetic field orientation), where the field orientation was such that it did not affect the gas compression. In the equipartition field strength simulation we find that the crossing shock has compressed the magnetic field to such an extent that $\beta \approx 0.1$. While it is evident from the magnetic field lines that in the weak-field case the strength of the magnetic field is greatly enhanced at the crossing shock, it is still extremely weak in comparison to the gas pressure. Even at the crossing shock, $\beta \approx 10^5$ in the weak-field jet. As a second example, note the low-density region surrounding the jet beam in the weak-field simulation. No such region occurs in the $\beta_i = 1$ simulation. The highly uniform spacing of field lines in the $\beta_i = 1$ simulation suggests that we can again ascribe the origin of this difference to the magnetic pressure. The effects of the magnetic pressure also appear when one considers the postshock density of material that passes through the oblique section of the bow shock. The postshock density of the weak-field simulation is about a factor of 3 larger than in the $\beta_i = 1$ simulation. In the case of the initially equipartition field strength simulation, $\beta < 1$ in this region of the flow, showing that the magnetic pressure indeed can have a strong influence on the postshock compression.

There are also strong effects on the jet due to pulsing. If we compare the high field pulsed-jet simulation to the steady jet shown in Figures 2*a* and 2*b*, with $\beta = 1$ initially, we immediately notice that the bow shock is much more streamlined in the case of the pulsed jet. We attribute this streamlining to the unsteady nature of the collisions between the internal working surfaces and the terminal working surface. Finally, as was mentioned earlier, the unshocked gas between the internal working surfaces rarefies as it propagates, cooling adiabatically. Thus, the sonic Mach number of the jet increases along the jet axis. The sonic Mach number in these jets increases from 20 to ~ 40 just upstream of the jet shock, or terminal working surface. It is also worth noting the increased number of closed field lines behind the bow shock in the weak-field simulation compared to the $\beta_i = 1$ simulation. This is in agreement with the trend noted earlier, that, as the strength of the magnetic field is increased, the occurrence of reconnection is reduced.

4.5. *Pulsed Jets: The Effect of Pulsation Amplitude*

In Figure 5 we compare two jet simulations, Pulse1 and Pulse1a, which differ only by the amplitude of the jet velocity variations. Our intention is to clarify the effects of these variations on the physical characteristics of the jet, and their dependence on the amplitude of the variations. Consider the rarefaction regions in the jet beam, between the pairs of internal working surfaces, whose origin was previously described. As was mentioned earlier, the velocity variations cause the gas between the internal working surfaces to undergo an adiabatic rarefaction, which at some point will be limited by radial motions due to an imbalance in the total, gas plus magnetic, pressure. In the 25% and 50% pulsed jets, this rarefaction resulted in a gas pressure reduction by factors of 10 and 100, respectively, and hence the parameter β is reduced to 0.25 and 0.1, respectively. This difference can be understood by considering the terms in the denominator of equation (19) which show us that the higher the pulse amplitude, the faster the rarefaction process will occur. As we just noted, however, this rarefaction process will eventually be terminated by radial gas motions, which is exactly what causes the compressional wave in the 50% pulsed-jet beam. This compressional wave is driven by an imbalance in the total pressure, gas plus magnetic, which differs by an order of magnitude across the wave front.

Next we compare the magnetic field lines expelled from the postshock region between the internal working surfaces for the two simulations. The images show that a higher pulse amplitude leads to a greater efflux of postshock material into the cocoon. This is quite reasonable, since the higher the pulse amplitude, the stronger the shock wave and the higher the postshock pressure. The gas that is driven out from between the postshock region of the internal working surfaces has an additional effect on the jet beam. As the internal working surfaces propagate down the jet beam the expelled gas pushes cocoon material ahead of it out of the way, leaving a wake of rarefied gas behind. This is the major factor leading to the difference in the density adjacent to the jet beam for the two simulations.

We can also see the effects of increased pulse amplitude by considering the jet head. In both simulations, a pulse has recently collided with the jet head. The maximum temperature in the simulations occurs in the jet head. This is about twice as large for the 50% pulse amplitude jet compared to the 25% simulation. Finally, note the numerous locally closed field loops caused by reconnection events in the 50% pulse amplitude simulation. Generally speaking, this contrast owes its origin to the greater violence associated with the collisions of the internal working surfaces with the terminal working surface in the 50% pulse amplitude case, when compared with the 25% simulation. Instabilities associated with each shock collision appear to increase the local turbulence in the flow in the jet head leading to more field reversals and reconnection.

5. DISCUSSION: MAGNETIC TENSION AND RECONNECTION

Our simulations demonstrate that while the global morphology of the jets is not strongly affected by initially equi-

partition strength poloidal magnetic fields, the details of the flow pattern can be changed. In addition, the presence of magnetic reconnection leads to a new means for transferring energy in the bulk flow into thermal energy in a way that does not directly involve shocks. We observe reconnection in our simulations in two distinct situations. The first is the dramatic, cooling-induced pinching off of field lines as the bow shock and jet shock collapse onto one another, shown in Figure 3*b* for an $\eta = 1$ jet. It should be noted that by increasing the jet velocity we can quickly enter a parameter regime where the cooling is insufficient to cause the bow shock and jet shock to collapse onto one another. In this case no reconnection occurs at the jet head for the magnetic field lines dragged out into the cocoon. The second situation in which we observe reconnection is the more-often-spoken-of situation, when a complex flow pattern folds over and pushes together opposed magnetic fields. This is observed most commonly in the pulsed jets, since these lead to the most complex flow patterns.

Regarding the first situation, an interesting question to ask is: "What strength magnetic field is necessary to inhibit the reconnection?" The obvious answer to this question is that for $\beta \ll 1$ the gas pressure can do little to compress the magnetic field and is only capable of bending the magnetic field for a very large radius of curvature. Therefore, reconnection will not occur, unless driven directly by the kinematics of the flow. Consider the description presented in § 4.1 on the early development of the shock pair for a top-hat jet and initially axial magnetic field. As described there, some small δt after the bow shock and jet shock are formed, a shock wave and a rarefaction wave will respectively propagate outward and inward radially. It is at this stage that for the most part we previously ignored the effects of the magnetic field on the kinematics since, $\beta \approx 10^2$ in the postshock region. We would require $\beta_i \approx 0.01$ in order to obtain $\beta \approx 1$ in the postshock region. For the $\eta = 5$ simulations presented, we do not resolve the cooling region but still find magnetic field lines dragged outward radially into the cocoon to an extent dependent on the strength of the magnetic field. As an example, in simulation Steady5 $\beta \approx 10$ in the postshock region, during the first 100 years or so, while $\beta_i = 0.1$, and the efflux of postshock gas is much less than that observed in the other simulations shown in Figures 2*a* and 2*b*.

In support of this discussion we now present a simple argument based on the order of magnitude of terms in the momentum equation. The MHD momentum conservation equation can be written in the following form:

$$\rho \frac{\partial \boldsymbol{u}}{\partial t} = -\rho(\boldsymbol{u} \cdot \nabla)\boldsymbol{u} - \nabla P_g + \frac{1}{c}(\boldsymbol{J} \times \boldsymbol{B}) . \tag{21}$$

We are interested in the relative balance of forces in the radial direction. A field reversal occurs when gas and the embedded magnetic field are drawn outward from the body of the jet by the combination of gas pressure and ram pressure terms. As the field lines are drawn out, the magnetic field in the postshock region will be reduced in magnitude, leading to a magnetic pressure force directed radially inward. In addition, since the field lines are anchored at the shock surface, the magnetic field lines will be bowed inward radially, leading to a tension force directed radially inward. A field reversal implies a strong folding of a field line. We take R_j to be the characteristic distance over which the gas pressure and magnetic pressure will vary. Note, however, that the radius of curvature for the field line that will act at the vertex of the loop will be of order of the stand-off distance D between the two shocks. Thus a field line that was originally parallel to the z-axis is "plucked" outward radially with the footpoints of the line connecting it to the jet separated by a distance D. The radius of curvature for the line will be $D/2$.

Transforming the Lorentz force term using equation (12) and considering only the scale of the gradient terms allows us to write the following condition for the Lorentz force overwhelming the other forces. We use the subscript 2 to refer to conditions behind the shocks:

$$\frac{B_2^2}{2\pi D} + \frac{B_2^2}{4\pi R_j} \geq \frac{\rho_2 u_{r,2}^2}{R_j} + \frac{P_{g,2}}{R_j} . \tag{22}$$

The magnetic field in the outward flowing gas can be found from flux conservation. If the majority of the field comes from jet gas outside some radii R_i then

$$\pi(R_j^2 - R_i^2)B_z = 2\pi R_j \left(\frac{D}{2}\right) B_2 , \tag{23}$$

so that

$$B_2 = \left(\frac{R_j^2 - R_i^2}{R_j D}\right) B_z . \tag{24}$$

To simplify this expression we substitute

$$R_i^2 = (1 - \lambda)R_j^2 , \tag{25}$$

for $\lambda > 0$, giving

$$B_2 = \left(\frac{\lambda R_j}{D}\right) B_z . \tag{26}$$

The other terms in equation (22) can be found from the strong, isothermal shock (sonic Mach number $M_s \gg 1$) relations: $\rho_2 = \rho_j M_s^2$; $P_{g,2} = \rho_j v_j^2$. The use of the isothermal conditions means this model is applicable for times $t > t_c$. Note also that we are assuming that the two components of the field in the loop (B_r and B_z) have approximately equal strength. For the radial flow velocity we write $u_{r,2} = \delta v_j$ where the simulations show that $\delta \leq 0.3$ is a typical value. Together, for $D \ll R_j$, we obtain

$$\beta \leq \frac{4\lambda^2}{\gamma M_s^2(1 + \delta^2 M_s^2)} \left(\frac{R_j}{D}\right)^3 . \tag{27}$$

The last piece of information needed is the stand-off distance between the two shocks. Falle & Raga (1993) provide an analysis of the flow between an internal working surface for pure hydrodynamic jets. Since we have found that the compression ratios behind the shocks in our simulations are not strongly affected by the magnetic fields, we use their result that $D = (e^{1/2}/2M_s)R_j$. With these relations we can derive the following relationship between the strength of the field (in terms of β) needed to retard the radial flow and the sonic Mach number:

$$\beta \leq \frac{32\lambda^2 M_s}{\gamma(1 + \delta^2 M_s^2)} \left(\frac{1}{e^{3/2}}\right) . \tag{28}$$

In the limit of strong shocks we find

$$\beta \leq \frac{32\lambda^2}{\gamma\delta^2 M_s}\left(\frac{1}{e^{3/2}}\right).$$

For the $M_s = 20$ (bow shock, jet shock) pair in the $\eta = 1$ simulations this gives a limit of $\beta < 0.2$. This matches very well with the observation, evident in Figure 2*b*, that only the $\beta_i = 0.1$ simulation showed a strong reduction in tangential motions and reconnection events.

We note also that our simulations showed that when field reversals did occur, reconnection did not happen until after a cooling time t_c. Strong cooling reduces the stand-off distance D, which is also the characteristic field scale of the field reversed region. The exact mechanism by which reconnection occurs is still a subject of considerable debate; however, our results concerning the rate of reconnection and the stand-off distance are easily understood in terms of a reconnection velocity $V_{\rm rec}$. This is the speed at which flux can be dragged into a reconnecting region. In the Sweet-Parker model (Parker 1979) this can be expressed in terms of the resistive diffusion coefficient η and the width, l, of the reconnection layer:

$$V_{\rm rec} = \frac{2\eta}{l}. \tag{29}$$

Since $l \leq D$, we see that one expects that reconnection will not occur for large stand-off distances. Consideration of $V_{\rm rec}$ for other forms of reconnection such as tearing mode (Vishniac & Lazarian 1999) yield similar conclusions.

6. CONCLUSION

To summarize, we have studied the evolution of steady and pulsed, radiative, magnetohydrodynamic jets for a range of parameters applicable to YSOs. Our simulations studied the specific case of an initially axial magnetic field with a strength characterized by the parameter $\beta_i = 0.1$–10^7. We find that the general characteristics of a RMHD jet with an embedded axial magnetic field do not differ from those of its hydrodynamic counterpart. Instead we find that the influence of the magnetic field is to modify the details of the flow. In particular we find that the fields can lead to an inhibition of instabilities, and increase in the "order" of the flow, and the introduction of magnetic reconnection.

We find that for the case of axial magnetic fields that are initially of equipartition strength or less, the postshock dynamics will be dominated by the hydrodynamics of the flow. This is due to the shock-induced increase in the thermal pressure and relatively small change to the magnetic field strength. The postshock flow between the bow shock and the jet shock can be understood, when $\beta \gg 1$, as a de Laval nozzle with radially ejected, postshock flow dragging out the embedded axial magnetic field into the cocoon, where it is susceptible to reconnection. When the cooling is sufficiently strong to cause the collapse of the bow shock and jet shock onto one another, the magnetic field lines dragged into the cocoon suffer magnetic reconnection.

For steady jets we find that axial magnetic fields have little effect on the postshock compression, or maximum density in the head of evolved jets. This is not a surprising result at all, since the bow shock and jet shock are never far from normal shocks, and the maximum compression will occur in regions where the shock is nearly normal to the flow. Instead we find that strong magnetic fields can inhibit the motion of complex flows in the head that would bend or twist the magnetic field. It is the tension associated with the field which is the agent of the inhibition. We also find a reduction in the occurrence of reconnection with the increase in the magnetic field strength.

With the introduction of jet pulsing, new features appear in the flow. We presented analytic arguments to predict the time and location of shock formation via Burgers's equation, finding a good agreement with the simulations. Similar arguments were used by Raga & Cantó (1998) to describe the formation of upstream to downstream density contrasts across internal working surfaces. Jet rarefaction between the sets of internal working surfaces leads to an increasingly magnetic field–dominated (i.e., β decreasing) jet with propagation. This may be an important point for jet stability as the rarefaction between the internal working surfaces leads to a decrease in the Alfvénic Mach number, which in linear perturbation theory controls the growth of Kelvin-Helmholtz instabilities. We have also found that the incorporation of pulsing into the jet has lead to increasingly complicated flow patterns and thereby an increased occurrence of magnetic reconnection.

By comparing pulsed jets with different pulse amplitudes we find a number of features of the flow which are directly dependent on the pulse amplitude. These include the time and location of shock formation, the rate of rarefaction between internal working surfaces, and the postshock temperatures and pressures during the collision of internal working surfaces with the terminal shock, to name a few. Generally speaking, the increased pulse amplitude shortens the timescale on which processes occur. It is interesting in this situation to ask what change we might expect if the jet pulsation amplitude and period varied with time. It is likely that the long-term evolution of the jet beam would show predominantly the features associated with the long timescales. That is, we expect weak, fast moving internal working surfaces to pass through stronger, slower moving internal working surfaces in the same way that the internal working surfaces studied in this work pass through the terminal shock, or jet shock.

Finally, the most important result we find is the existence of numerous reconnection sites in the flow. While it is not clear how the existence of reconnection would change in helical fields, our simulations show that the existence of a B_z component when coupled to the dynamics of shocks in jets naturally leads to conditions favorable for reconnection. Further work needs to be done to determine what role this will play in the energetics and, more importantly, the evolution of field topologies in the jet. Our simulations show that purely axial fields do not alter the propagation characteristics of the jets significantly. In Frank et al. (1998) and Cerqueira et al. (1997) it was shown that toroidal fields can have strong effects on the propagation characteristics leading to nose-cone morphologies. If such shapes do not occur in real jets, it is possible that reconnection is the agent allowing global changes in the jet field topologies. We note also that if instabilities grow faster than cooling timescales in the flow, they can be an important driver for reconnection.

With the move from two-dimensional cylindrically symmetric to three–dimensional MHD simulations we can expect the flow patterns in jet simulations to become

increasingly complicated. The effects that this may have on the rate of magnetic reconnection and the effects that reconnection may have on the stability of the flow are very interesting issues that need to be considered. Of particular interest would be a self-consistent calculation of the X-ray luminosity expected from magnetic reconnection.

We wish to thank Thibaut Lery, Guy Delamarter, and Arieh Königl for helpful discussion of this project. This work was supported at the University of Rochester by NSF grant AST 09-78765 and the University of Rochester's Laboratory for Laser Energetics. Work by T. W. J. was supported by NSF grants INT95-11654, AST 96-19438, and AST 96-16964, by NASA grant NAG 5-5055, and by the University of Minnesota Supercomputing Institute. The work by D. R. was supported in part by KOSEF through grant 981-0203-011-2.

REFERENCES

Blandford, R. D., & Payne, D. G. 1982, MNRAS, 199, 883
Blondin, J. M., Fryxell, B. A., & Königl, A. 1990, ApJ, 360, 370
Bührke, T., Mundt, R., & Ray, T. P. 1988, A&A, 200, 99
Cantó, J., & Rodríguez, L. F. 1980, ApJ, 239, 982
Cerqueira, A. H., de Gouveia Dal Pino, E. M., & Herant, M. 1997, ApJ, 489, L185
Dalgarno, A., & McCray, R. A. 1972, ARA&A, 10, 375
de Gouveia Dal Pino, E. M., & Benz, W. 1994, ApJ, 435, 261
Delamarter, G., Frank, A., & Hartmann, L. 2000, ApJ, in press
Falle, S. A. E. G., & Raga, A. C. 1993, MNRAS, 261, 573
Frank, A., Gardiner, T. A., Delamarter, G., Betti, R., & Lery, T. 1999, ApJ, submitted
Frank, A., & Mellema, G. 1996, ApJ, 472, 684
Frank, A., Noriega-Crespo, A., Ryu, D., & Jones, T. W. 1997, in IAU Symp. 182, Low Mass Star Formation: From Infall to Outflow (poster proceedings), ed. F. Malbet & A. Castets (Dordrecht: Kluwer), 115
Frank, A., Ryu, D., Jones, T. W., & Noriega-Crespo, A. 1998, ApJ, 494, L79
Harten, A. 1983, J. Comput. Phys., 49, 357
Jones, T. W., Gaalaas, J. B., Ryu, D., & Frank, A. 1997, ApJ, 482, 230
Königl, A. 1989, ApJ, 342, 208
Kudoh, T., Matsumoto, R., & Shibata, K. 1998, ApJ, 508, 186
Landau, L. D., & Lifshitz, E. M. 1997, Fluid Mechanics (Oxford: Butterworth-Heinemann)
LeVeque, R. J. 1992, Numerical Methods for Conservation Laws (Boston: Birkhauser)
———. 1997, in Proc. 27th Saas-Fée Course of the Swiss Society of Astrophysics and Astronomy (New York: Springer), 1
Mac Low, M., Klessen, R. S., Burkert, A., & Smith, M. D. 1998, Phys. Rev. Lett., 80, 2754
Micono, M., Massaglia, S., Bodo, G., Rossi, P., & Ferrari, A. 1998, A&A, 333, 1001
Norman, M. L., Winkler, K. H., & Smarr, L. 1983, in Astrophysical Jets, ed. J. Centrella, J. LeBlanc, & R. Bowers (Boston: Jones & Bartlett), 88
Ouyed, R., & Pudritz, R. E. 1993, ApJ, 419, 255
———. 1997, ApJ, 482, 712
Parker, E. N. 1979, Cosmical Magnetic Fields (Oxford: Clarendon)
Porter, D. H., & Woodward, P. R. 1994, ApJS, 93, 309
Raga, A. C. & Cantó, J. 1998, Rev. Mexicana Astron. Astrofis., 34, 73
Raga, A. C., Cantó, J., Binette, L., & Calvet, N. 1990, ApJ, 364, 601
Raga, A. C., & Kofman, L. 1992, ApJ, 386, 222
Ray, T. P., Muxlow, T. W. B., Axon, D. J., Brown, A., Corcoran, D., Dyson, J., & Mundt, R. 1997, Nature, 385, 415
Rees, M. J. 1978, MNRAS, 184, 61P
Reipurth, B. 1989, Nature, 340, 42
Reipurth, B., Bally, J., & Devine, D. 1997, AJ, 114, 2708
Romanova, M. M., Ustyugova, G. V., Koldoba, A. V., Chechetkin, V. M., & Lovelace, R. V. E. 1998, ApJ, 500, 703
Ryu, D., & Jones, T. W. 1995, ApJ, 442, 228
Ryu, D., Jones, T. W., & Frank, A. 1995a, ApJ, 452, 785
Ryu, D., Yun, H. S., & Choe, S. 1995b, J. Korean Astron. Soc., 28, 243
Ryu, D., Miniati, F., Jones, T. W., & Frank, A. 1998, ApJ, 509, 244
Schwartz, R. D. 1975, ApJ, 195, 631
Shu, F. 1997, in IAU Symp. 182, Herbig-Haro Flows and the Birth of Low-Mass Stars, ed. B. Reipurth & C. Bertout (Dordrecht: Kluwer)
Smith, M. D., Suttner, G., & Zinnecker, H. 1997, A&A, 320, 325
Stone, J. M., & Norman, M. L. 1993, ApJ, 413, 210
Stone, J. M., Ostriker, E. C., & Gammie, C. F. 1998, ApJ, 508, L99
Stone, J. M., Xu, J., & Hardee, P. E. 1997, ApJ, 483, 136
Strang, G. 1968, SIAM J. Numer. Anal., 5, 506
Thomas, J. H. 1988, ApJ, 333, 407
Vishniac, E. T., & Lazarian, A. 1999, ApJ, 511, 193
Zinnecker, H., McCaughrean, M. J., & Rayner, J. T. 1998, Nature, 394, 862